COMPLEX OXIDES

Extreme tensile strain states in La$_{0.7}$Ca$_{0.3}$MnO$_3$ membranes

Seung Sae Hong[1,2,3]*, Mingqiang Gu[4,5], Manish Verma[6], Varun Harbola[2,7], Bai Yang Wang[2,7], Di Lu[2,4,7], Arturas Vailionis[8,9], Yasuyuki Hikita[2], Rossitza Pentcheva[6], James M. Rondinelli[4], Harold Y. Hwang[1,2]

A defining feature of emergent phenomena in complex oxides is the competition and cooperation between ground states. In manganites, the balance between metallic and insulating phases can be tuned by the lattice; extending the range of lattice control would enhance the ability to access other phases. We stabilized uniform extreme tensile strain in nanoscale La$_{0.7}$Ca$_{0.3}$MnO$_3$ membranes, exceeding 8% uniaxially and 5% biaxially. Uniaxial and biaxial strain suppresses the ferromagnetic metal at distinctly different strain values, inducing an insulator that can be extinguished by a magnetic field. Electronic structure calculations indicate that the insulator consists of charge-ordered Mn^{4+} and Mn^{3+} with staggered strain-enhanced Jahn-Teller distortions within the plane. This highly tunable strained membrane approach provides a broad opportunity to design and manipulate correlated electron states.

Externally driven changes in atomic spacing offer access to distinct phases and functionalities of materials. In complex oxides (1–3), strain can be used to manipulate quantum states of matter (4–8) because the electrons in these materials and their correlated interactions are tightly coupled to the lattice. However, bulk oxide crystals are typically brittle and crack under relatively small tensile strain; larger strain states are usually only accessible under compression (9). Although epitaxial strain imparted by lattice mismatch between a thin film and the underlying substrate can modulate the properties of thin films (5, 6, 10, 11), the discrete lattice parameters of available substrates (10), combined with strain-driven defect formation during high-temperature synthesis (12, 13), present fundamental limitations to exploring how extreme and coherent strain fields affect correlated states in oxides. The recent development of free-standing complex oxide membranes (14) both circumvents these challenges and provides unique opportunities to realize previously unobserved strain-induced responses. Oxide membranes can be mechanically coupled to an external platform without an epitaxial relationship, for which strain states of different symmetries can be freely chosen by design. Moreover, the critical fracture strain is often greatly enhanced for small materials length scales (15, 16), enabling a viable route to impart large tensile strain states well beyond the typical values that ceramics can withstand.

Rare-earth perovskite manganites are correlated electron systems with multiple phases coupled to the lattice (17). A number of stable electronic and magnetic ground states arise at different carrier concentrations, as structural Jahn-Teller distortions to the MnO$_6$ octahedra generate different bond network configurations, which therefore change the magnetic exchange interactions between 3d electrons on neighboring sites. Here, we focused on La$_{0.7}$Ca$_{0.3}$MnO$_3$ (LCMO), a representative colossal magnetoresistance (CMR) material (17) with a transition between a low-temperature ferromagnetic metal (FM-M) and a high-temperature paramagnetic insulator (PM-I) at a Curie temperature T_C ~ 250 K. The metallic ground state of LCMO is closely adjacent to many other phases, such as charge/orbital ordering (COO), a ferromagnetic insulating state, and antiferromagnetic states, thereby offering an ideal testbed to understand electronic correlations controlled by elastic lattice strain.

Using pulsed laser deposition (PLD), we synthesized multilayer heterostructures consisting of SrCa$_2$Al$_2$O$_6$ (used as a sacrificial layer), SrTiO$_3$, and LCMO (fig. S1) to release free-standing LCMO nanomembranes. The solid-solution family of (Ba,Sr,Ca)$_3$Al$_2$O$_6$ enables the continuous tuning of the sacrificial layer lattice constant from 0.382 nm (Ca 100%) to 0.413 nm (Ba 100%), covering the lattice constant range of the vast majority of perovskite and related oxides (18, 19). SrCa$_2$Al$_2$O$_6$, a particular composition for the sacrificial layer developed for this experiment instead of Sr$_3$Al$_2$O$_6$ used previously (14), is nearly perfectly lattice-matched (<0.1%) to the LCMO lattice constant (a = 0.386 nm). We found that minimizing lattice mismatch is a critical factor to avoid crack formation in the released mem-

branes (fig. S2) and is therefore essential to achieve homogeneous tensile strain states over large areas. The LCMO layer was kept at a minimum of 10 unit cells to avoid the Berezinskii-Kosterlitz-Thouless crystalline melting transition previously observed in the ultrathin limit (20). All heterostructures were grown epitaxially and monitored by in situ reflection high-energy electron diffraction (RHEED). By selectively dissolving the sacrificial layer in water, the top oxide film was detached from the substrate and transferred onto a polyimide sheet, which we used as a stretchable substrate (21).

The strain state of the oxide membrane can be controlled by external forces (Fig. 1A). The four sides of the polymer layer were clamped and stretched by micromanipulators with ~0.1% precision. The strong adhesion between the oxide membrane and the polymer layer provides efficient strain transfer to the oxide membrane without any observable slippage. The macroscopic size of the membrane (area > 10 mm^2) provides a uniform interior distribution of strain ε upon stretching and minimizes the edge effects observed in microflakes of exfoliated crystals (22). Finite-element analysis of the strained membrane/polyimide bilayer (Fig. 1A) indicated that the membrane area experiences a strain gradient near the membrane edges, whereas the majority of the membrane area at the center is homogeneously strained (Δε < 0.2%). The strained oxide/polymer bilayer was then glued onto a solid substrate such that the strain field was fixed even after the external force was removed (fig. S3) (21). The adhesive (polycaprolactone) used here can be reversibly melted by gentle heating (T < 100°C) on the sample assembly stage. Thus, it is possible to set and probe multiple strain states of the same membrane sample. Smaller strains less than 3% could be reset to the zero strain state by melting and releasing the adhesive, whereas higher strain states could only be stretched further in an irreversible manner thanks to the plastic deformation of the outer polymer layer (Fig. 1A). We found that the strain remains fixed for at least a week, down to cryogenic temperatures (T = 2 K) and under x-ray exposure, providing a versatile platform for multiple experiments.

We first optically characterized the strained membrane and found that the membrane reaches extreme macroscopic strain states. Two optical images, taken before and after establishing uniaxial tensile strain, are compared in Fig. 1B to estimate the strain. (Note here that a small tensile stress is also applied in the perpendicular direction to prevent compression by the finite Poisson ratio.) Because the oxide membrane is nearly transparent on the polyimide layer, we measured the strain by tracking the spacing of evaporated metal (Au) markers. By stretching oxide membranes

[1]Department of Applied Physics, Stanford University, Stanford, CA 94305, USA. [2]Stanford Institute for Materials and Energy Sciences, SLAC National Accelerator Laboratory, Menlo Park, CA 94025, USA. [3]Department of Materials Science and Engineering, University of California, Davis, CA 95616, USA. [4]Department of Materials Science and Engineering, Northwestern University, Evanston, IL 60208, USA. [5]Department of Physics, Southern University of Science and Technology, Shenzhen 518055, China. [6]Department of Physics and Center for Nanointegration (CENIDE), University of Duisburg-Essen, 47053 Duisburg, Germany. [7]Department of Physics, Stanford University, Stanford, CA 94305, USA. [8]Stanford Nano Shared Facilities, Stanford University, Stanford, CA 94305, USA. [9]Department of Physics, Kaunas University of Technology, LT-51368 Kaunas, Lithuania.
*Corresponding author. Email: sshong@ucdavis.edu

of different thickness d, we found that thicker membranes ($d > 20$ nm) undergo mechanical fracture under relatively small uniaxial tensile strains (<2%), as seen in optical images showing periodic crack formation (fig. S4). In contrast, ultrathin oxide membranes ($d < 10$ nm) could be stretched much more (>2%) without fracture.

Although the macroscopic strain state was visibly evident, we next assessed whether such large strains in the oxide membrane induce elastic or plastic deformation. We used grazing incident x-ray diffraction (GIXRD) to measure the change of the in-plane lattice constants. In an unstretched LCMO membrane, the perovskite (200) peak in a 2θ-ω scan corresponded to that of the bulk LCMO crystal. With increasing tensile strain, the GIXRD peak shifted
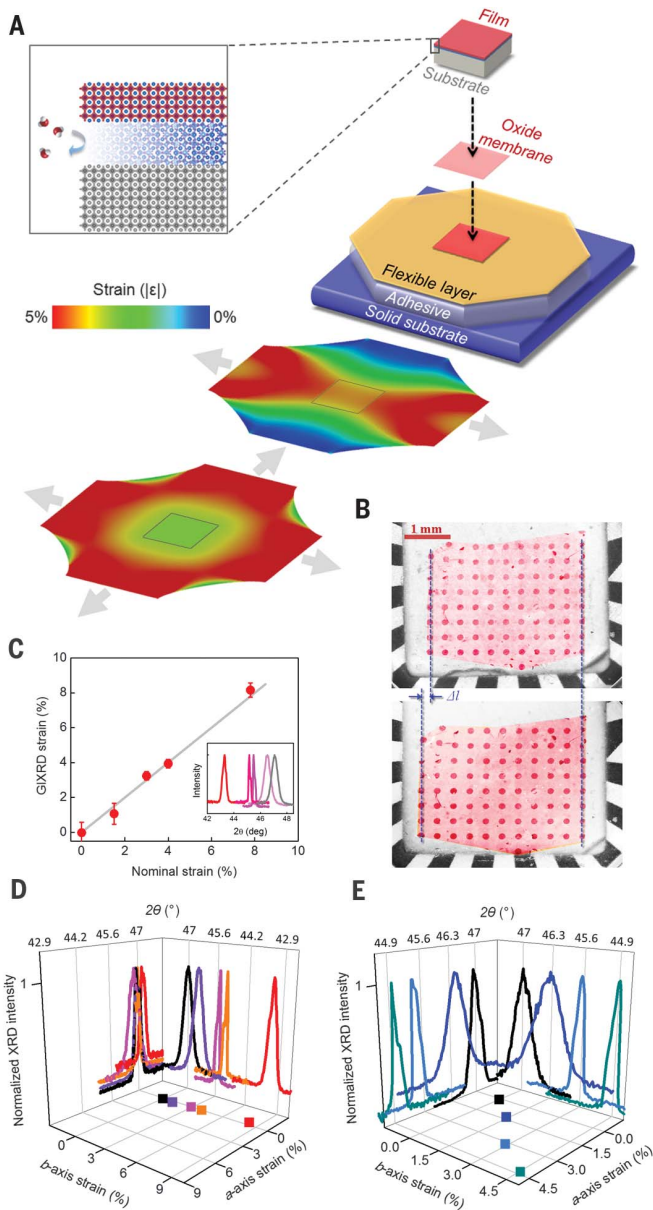
Fig. 1. Designer strain in 2D oxide membranes. (**A**) Schematic platform for straining oxide membranes. The lower maps plot finite-element analysis strain profiles of the polyimide/oxide bilayer under uniaxial and biaxial stress (*21*). The gray square in the strain maps indicates the boundary of the oxide membrane, beyond which only the polyimide remains. Inset: Lifting off a membrane from the substrate by etching a water-soluble layer in oxide heterostructures. (**B**) Optical microscope images of a 6-nm-thick LCMO membrane before (top) and after (bottom) stretching uniaxially. The ceramic chip carrier is used as a reference frame to optically characterize the strain state. (**C**) GIXRD strain as a function of the nominal strain observed optically. Error bars denote SD. Inset: GIXRD data of the LCMO (200) peak shifted by strain. (**D** and **E**) In-plane lattice changes and corresponding 2θ peaks of LCMO membranes characterized by GIXRD, for uniaxial (**D**) and biaxial (**E**) strain.
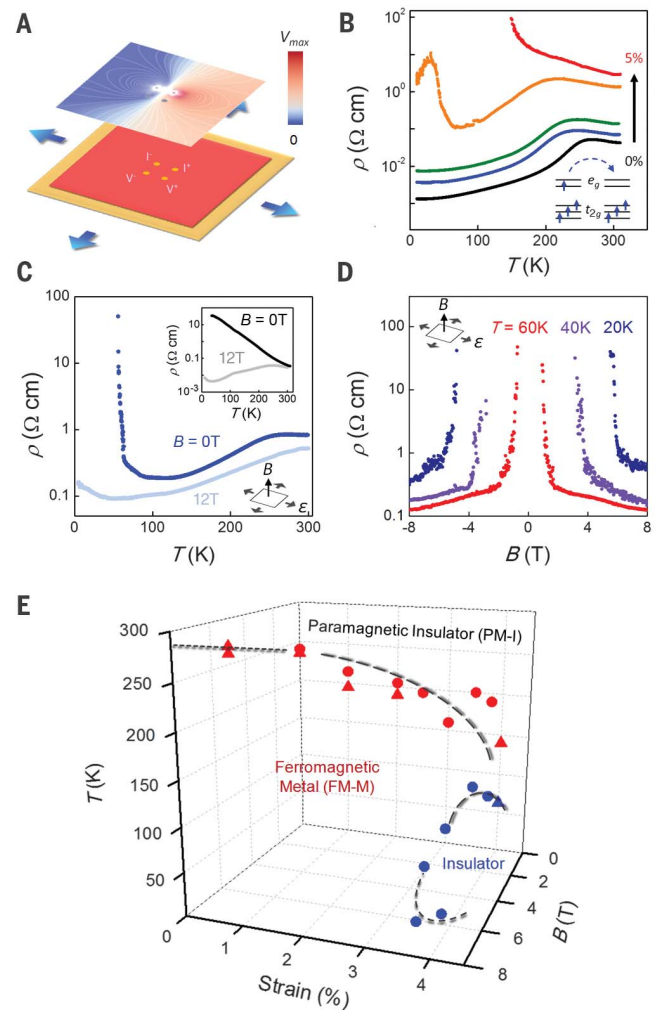
Fig. 2. Magnetotransport and phase diagram of biaxially strained La$_{0.7}$Ca$_{0.3}$MnO$_3$ membranes. (**A**) Electric potential mapping of the central vdP geometry in membranes. The boundary conditions were current nonpermeability at the edges; I^+ and I^- represent the current source and current sink. The voltage at V^- is held at $V = 0$, and V_{max} is calculated at V^+. (**B**) Evolution of the temperature-dependent resistivity of an 8-nm-thick LCMO membrane as a function of strain: 0% (black), 1% (blue), 2% (green), 4% (orange), and 5% (red) biaxial strain. No thickness dependence was observed between membranes of $d = 4$ nm and $d = 8$ nm (fig. S6). Inset: Double exchange interaction between two Mn sites. (**C**) Resistivity-temperature curves of a strained LCMO membrane ($d = 4$ nm, $\varepsilon = 3.5\%$) under perpendicular magnetic field. Inset: Resistivity-temperature curves of a LCMO film ($d = 4$ nm) grown on an SrTiO$_3$ (001) substrate under perpendicular magnetic field. (**D**) Magnetoresistance of the 4-nm-thick LCMO membrane shown in (C) at different temperatures. (**E**) Phase diagram of biaxially strained LCMO membranes. The phase boundaries are determined by resistive transitions during cooling curves ($B = 0$ T or $B = 5$ T with zero strain) and magnetoresistance data during increasing field sweeps ($T = 5$ K), acquired from membranes of two different thicknesses (circles, $d = 4$ nm; triangles, $d = 8$ nm).

to lower angles (Fig. 1C, inset), tracking the increase of the in-plane lattice constant. The strain values measured by the GIXRD scans closely matched the macroscopic strain observed in the optical images (Fig. 1C). The maximum tensile strain in the uniaxial geometry was 8.2% (a = 0.417 nm), far beyond typical tensile strains accessible in crystalline oxides [such as typical piezoelectrically induced strains up to ~1% (7)] and epitaxial strains in canonical oxide thin films up to ~3% (23). [It is again worth noting that for high-temperature synthesis, defect densities in such ionic materials often vary with strain (12, 13).] In addition, the symmetry of the strain field can be directly controlled. In Fig. 1, D and E, we present two examples for which the strain is independently tuned along different directions: asymmetric uniaxial strain states and symmetric biaxial strain states,

respectively. The ability to design both the magnitude and symmetry of the strain field— for example, through linear combinations of the two aforementioned states—opens up avenues for the manipulation of complex oxide membranes hosting electrons sensitive to orbital symmetry and filling.

We next leveraged access to these extreme strain states to both modulate the transport properties of LCMO and stabilize a non-equilibrium phase of the LCMO membranes under biaxial strain. First, we measured the membrane resistivity using van der Pauw (vdP) electrodes near the center of the membrane (Fig. 2A). In the central vdP configuration, the distribution of electric current is quite insensitive to the geometry and strain gradient of the membrane edge (fig. S5) (21). This requires that the membranes are large with respect to the vdP dimensions, which is easily achieved here with millimeter-scale membranes. Therefore, the electronic transport measurements accurately reflect the intrinsic response of the central area with homogeneous strain. The temperature-dependent resistivity $\rho(T)$ in the zero strain state exhibited T_C ~ 250 K, defined by the peak in $d[\log(\rho)]/d(T)$, consistent with prior studies. Next, by repeatedly stretching the membrane in a symmetric (biaxial) manner, we acquired the full evolution of $\rho(T)$ from the same oxide membrane at different strain states (Fig. 2B). We found that 5% biaxial tensile strain led to an increase in $\rho(300 \text{ K})$ by more than two orders of magnitude. Moreover, T_C of the FM-M/PM-I phase transition shifted to lower temperatures. These observations are consistent with the reduction of the in-plane orbital overlap between Mn d orbitals and O p orbitals under tensile strain, which is supported by our electronic structure calculations. The marked resistivity increase at room temperature evidences the reduced bandwidth and smaller hopping integral for itinerant electrons. In double exchange, the hopping e_g electron is forced to align with the other core t_{2g} electrons by a large Hund's-rule coupling (Fig. 2B, inset). Thus, the electronic bandwidth is modulated by the spin orientation between Mn sites and gives an effective ferromagnetic interaction mediated by the electronic conduction. The smaller electronic hopping integral directly suppresses the double-exchange interaction, moving the phase boundary to substantially lower temperatures (24).

In addition to the large shift in T_C, we found an unexpected insulating phase emerging at high biaxial strain states (>3%) at low temperatures. The insulating state below T = 70 K can be quenched by magnetic fields with a large negative magnetoresistance (Fig. 2, C and D) and magnetic field hysteresis (fig. S7). This insulator-to-metal transition upon the application of magnetic field qualitatively resembles

Fig. 3. Magnetotransport and phase diagram of uniaxially strained La₀.₇Ca₀.₃MnO₃ membranes. (**A**) Electric potential mapping of the central vdP geometry in membranes under a uniaxial strain, with 1:100 resistivity anisotropy. The boundary conditions were current nonpermeability at the edges; I^+ and I^- represent the current source and current sink. The voltage at V^- is held at V = 0, and V_{max} is calculated at V^+. (**B**) Room-temperature resistances R_{RT} (T = 290 K) in the central vdP geometry with different uniaxial strains. Open circles are resistances parallel to the strain direction; solid circles are resistances perpendicular to the strain direction. (**C** and **D**) Evolution of the temperature-dependent resistance of an 8-nm-thick LCMO membrane, parallel (C) and perpendicular (D) to the uniaxial strain of 0% (black), 1% (purple), 3% (blue), 5% (green), 7% (orange), and 8% (red). Each resistance-temperature curve is normalized by R_{RT} and is shifted vertically for visual clarity. (**E**) Resistance-temperature curves of the strained LCMO membrane (vdP resistance perpendicular to the strain ε = 8%) under perpendicular magnetic field. (**F**) Magnetoresistance of the LCMO membrane under perpendicular magnetic field at different temperatures. (**G**) Phase diagram of uniaxially strained LCMO membranes. The phase boundaries are determined by resistive transitions during cooling curves (B = 0 T or B = 5 T with zero strain) and magnetoresistance data during increasing field sweeps (T = 10 K), acquired from vdP resistances parallel (open circles) and perpendicular (solid circles) to the strain direction.
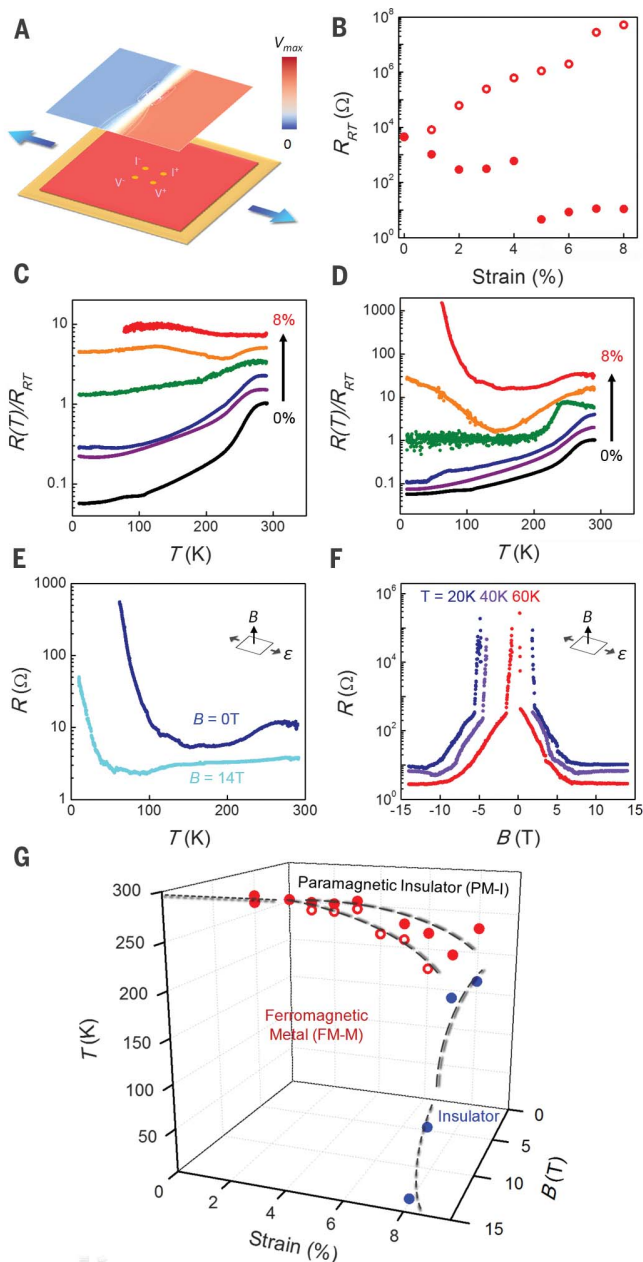
the field-induced melting of COO in competition with the FM-M. Similar behavior has been observed in low-bandwidth manganites (25). However, here the phase arises in a very different physical parameter space (temperature, strain, and resistivity) from prior reports of bulk crystals and epitaxially strained thin films of similar doping (see also Fig. 2C, inset) (26). On the basis of these structural and electrical studies, we constructed a phase diagram of LCMO as a function of biaxial strain and magnetic field (Fig. 2E).

In addition to the biaxial strain states, we investigated electronic transport of the LCMO membrane under different uniaxial strains from 1% to 8% (Fig. 3A and fig. S8). We first observed that the vdP resistances of two directions, parallel and perpendicular to the uniaxial strain direction, are substantially different with large resistance anisotropy up to 10^7 (Fig. 3B). Electrostatic simulations on the finite-size vdP geometry (fig. S9) can be used to convert the maximum resistance anisotropy to a resistivity anisotropy (~10^3). For such large anisotropies, the measurement is much more sensitive to the finite-size boundary conditions than the biaxial case. Therefore, we report the directly measured resistance, from which the resistivities can be deduced (21). The temperature-dependent resistances $R(T)$ of the two different directions were measured for a series of uniaxial strain states (Fig. 3, C and D), showing the reduction of T_C by increasing strain. Nonmetallic temperature dependence in resistance-temperature curves first appears in the resistance parallel to the strain (ε = 6 to 8%) and is observed in the perpendicular direction at larger strains (ε = 7 to 8%). The insulating states for high uniaxial strains (T < 150 K, ε = 7 to 8%) are largely suppressed upon the application of magnetic field and show very large magnetoresistance (Fig. 3, E and F), similar to the biaxial strain states above 3%. The phase diagram of uniaxially strained LCMO membranes based on these electrical studies (Fig. 3G) qual-

itatively resembles the biaxial phase diagram (Fig. 2E) with the addition of a bifurcation of the resistively measured transition along the two different directions with respect to the strain direction.

We next performed density functional theory (DFT) calculations to consider the microscopic origin of the strain-induced insulating state. We first modeled LCMO using a model with ordered La^{3+} and Ca^{2+} cations (rather than a solid-solution configuration) in a ratio of 2:1 on the perovskite A-cation site to find the ground state (27). We applied both uniaxial and biaxial tensile strain up to 8%. A strain condition was not imposed for the out-of-plane lattice direction, and it was allowed to computationally relax. We then compared the ground-state energies of two phases—the FM-M phase and an antiferromagnetic insulator (AFM-I) phase with A-type ordering—at different strain states (Fig. 4A). The bulk DFT-relaxed FM-M phase was ~45 meV per formula unit (f.u.) lower in energy than the AFM-I phase, consistent with the experimental bulk phase diagram. The half-metallic behavior held for the FM-M phase throughout the examined strain level, as seen from the electronic density of states (Fig. 4B). We found that the energy difference between the two states decreases with increasing tensile strain until reaching a critical value $\varepsilon^* \approx$ 7% (uniaxial), 3% (biaxial), at which point a FM-M to AFM-I transition occurs, in good agreement with the experimental results. Beyond this point, the AFM-I phase is stabilized and characterized by a COO insulating state (Fig. 4C) for both uniaxial and biaxial strain configurations. In the AFM-I state, ordering of $Mn^{4+}O_6$ and Jahn-Teller–distorted $Mn^{3+}O_6$ octahedra is found (Fig. 4D). By modeling various configurations for the A-site to simulate solid solutions with random La/Ca site occupancy, we found that the stripe-type COO (fig. S10) is robust to the A-site chemical distribution (21) (fig. S11). The DFT calculations confirm that the experimentally observed insulating phase under high strain is the A-type

AFM-I phase with a stripe COO. For the one-third–doped LCMO, such a stripe COO was predicted with a two-dimensional model Hamiltonian that includes double-exchange and Jahn-Teller phonons (28), but different ground states were observed in epitaxial films (29, 30). Although the detailed microscopic structure remains to be investigated, it is striking that such an anisotropic state is stabilized for both uniaxial and biaxial strain.

The FM-M phase is stable at low-strain states because the smaller in-plane lattice constants favor reduced Q_3 Jahn-Teller distortions of the MnO_6 octahedra (four short and two long Mn-O bonds, shown schematically in Fig. 4A) and more uniform Mn-O-Mn bond angles (31). In contrast, the COO AFM-I exhibits inequivalent Mn^{4+}/Mn^{3+} sites, forming an ordered structure controlled by the long Mn-O bond from the Q_3 Jahn-Teller distortion (fig. S10). The long Mn-O bond network is staggered in an alternating manner along ⟨110⟩ with respect to the orthorhombic lattice vectors, in which the longer Mn-O bond is elastically favored by larger in-plane lattice constants achieved through large tensile strains in the LCMO membranes. Furthermore, under extreme strain, superexchange interactions and electron localization (from weakened orbital overlap) dominate over metallic double exchange and stabilize the AFM-I ground state, which is consistent with the observed magnetic field–induced insulator-to-metal transitions (Figs. 2C and 3E).

The ability to achieve tensile strains in a continuous manner, complementing compressive strain states set by hydrostatic pressure (9), offers a vast unexplored phase space to control atomic spacing in correlated electron systems. The example of LCMO membranes demonstrates that a macroscopic, crack-free oxide membrane can be synthesized using a lattice tunable sacrificial layer, and is applicable to a large set of complex oxide materials to which large and uniform tensile strains can be applied. The access to such extreme tensile strain states, available in nanoscale oxide
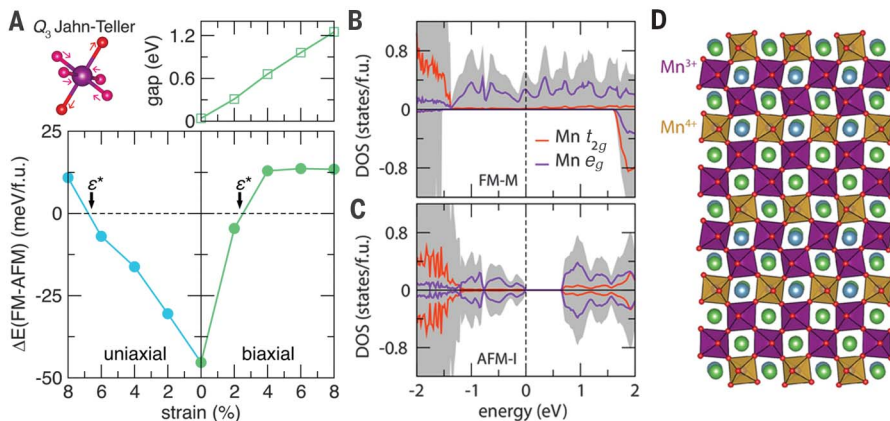

Fig. 4. Strain stabilization of insulating LCMO.
(**A**) DFT total energy difference between the ferromagnetic metallic (FM-M) and antiferromagnetic insulating (AFM-I) phases with respect to uniaxial and biaxial strain in $La_{2/3}Ca_{1/3}MnO_3$. Schematic (top left) shows that Q_3 Jahn-Teller distortion of the MnO_6 octahedra active in the AFM-I phase drives the FM-M to AFM-I transition at the critical strain value ε^* indicated by the bold vertical arrows. Increasing biaxial strain increases the bandgap of the insulating phase. (**B** and **C**) Electronic density of states for LCMO at 4% biaxial strain in the FM-M (B) and AFM-I (C) phases. (**D**) The AFM-I state displays charge-ordered Jahn-Teller–distorted $Mn^{3+}O_6$ (purple) and $Mn^{4+}O_6$ (orange) octahedra (see also fig. S10).

membranes, offers great opportunities to vary fundamental parameters and energy scales wherever competing orders exist, which may enable theory-based design and experimental exploration of phases beyond those in bulk equilibrium materials. Beyond complex oxides, the strain approach demonstrated here can be broadly applied to strain engineering of free-standing 2D layers, including 2D van der Waals materials (*32*) and compound semiconductor membranes (*33*).

REFERENCES AND NOTES

1. M. Imada, A. Fujimori, Y. Tokura, *Rev. Mod. Phys.* **70**, 1039–1263 (1998).
2. B. Keimer, S. A. Kivelson, M. R. Norman, S. Uchida, J. Zaanen, *Nature* **518**, 179–186 (2015).
3. H. Y. Hwang et al., *Nat. Mater.* **11**, 103–113 (2012).
4. L. Gao et al., *Phys. Rev. B* **50**, 4260–4263 (1994).
5. J. P. Locquet et al., *Nature* **394**, 453–456 (1998).
6. I. Bozovic, G. Logvenov, I. Belca, B. Narimbetov, I. Sveklo, *Phys. Rev. Lett.* **89**, 107001 (2002).
7. C. W. Hicks et al., *Science* **344**, 283–285 (2014).
8. H.-H. Kim et al., *Science* **362**, 1040–1044 (2018).
9. A. Jayaraman, *Rev. Mod. Phys.* **55**, 65–108 (1983).
10. D. G. Schlom et al., *MRS Bull.* **39**, 118–130 (2014).
11. Q. Gan, R. A. Rao, C. B. Eom, J. L. Garrett, M. Lee, *Appl. Phys. Lett.* **72**, 978–980 (1998).
12. C. Thiele, K. Dörr, O. Bilani, J. Rödel, L. Schultz, *Phys. Rev. B* **75**, 054408 (2007).
13. U. Aschauer, R. Pfenninger, S. M. Selbach, T. Grande, N. A. Spaldin, *Phys. Rev. B* **88**, 054111 (2013).
14. D. Lu et al., *Nat. Mater.* **15**, 1255–1260 (2016).
15. M. D. Uchic, D. M. Dimiduk, J. N. Florando, W. D. Nix, *Science* **305**, 986–989 (2004).
16. A. Banerjee et al., *Science* **360**, 300–302 (2018).
17. Y. Tokura, *Rep. Prog. Phys.* **69**, 797–851 (2006).
18. A. K. Prodjosantoso, B. J. Kennedy, B. A. Hunter, *Aust. J. Chem.* **53**, 195–202 (2000).
19. P. Singh et al., *ACS Appl. Electron. Mater.* **1**, 1269–1274 (2019).
20. S. S. Hong et al., *Sci. Adv.* **3**, eaao5173 (2017).
21. See supplementary materials.
22. Z. Liu et al., *Nat. Commun.* **5**, 5246 (2014).
23. C. Adamo et al., *Appl. Phys. Lett.* **95**, 112504 (2009).
24. H. Y. Hwang, T. T. M. Palstra, S.-W. Cheong, B. Batlogg, *Phys. Rev. B* **52**, 15046–15049 (1995).
25. Y. Tomioka, A. Asamitsu, H. Kuwahara, Y. Moritomo, Y. Tokura, *Phys. Rev. B* **53**, R1689–R1692 (1996).
26. J. Zhang et al., *Nat. Mater.* **15**, 956–960 (2016).
27. S. Mori, C. H. Chen, S. W. Cheong, *Nature* **392**, 473–476 (1998).
28. T. Hotta, A. Feiguin, E. Dagotto, *Phys. Rev. Lett.* **86**, 4922–4925 (2001).
29. J. Klein et al., *Phys. Rev. B* **66**, 052414 (2002).
30. M. Ziese, H. C. Semmelhack, K. H. Han, *Phys. Rev. B* **68**, 134444 (2003).
31. F. Rivadulla, M. A. López-Quintela, J. Mira, J. Rivas, *Phys. Rev. B* **64**, 052403 (2001).
32. K. S. Novoselov, A. Mishchenko, A. Carvalho, A. H. Castro Neto, *Science* **353**, aac9439 (2016).
33. J. A. Rogers, M. G. Lagally, R. G. Nuzzo, *Nature* **477**, 45–53 (2011).
34. Data and computational codes are available at Zenodo (doi:10.5281/zenodo.3653340).
35. Computational codes are available at Zenodo (doi:10.5281/zenodo.3647659).
36. Computational codes are available at Zenodo (doi:10.5281/zenodo.3648630).

Science

Extreme tensile strain states in La$_{0.7}$Ca$_{0.3}$MnO$_3$ membranes

Seung Sae Hong, Mingqiang Gu, Manish Verma, Varun Harbola, Bai Yang Wang, Di Lu, Arturas Vailionis, Yasuyuki Hikita, Rossitza Pentcheva, James M. Rondinelli and Harold Y. Hwang

Straining an oxide membrane

Perovskite manganites, such as La$_{0.7}$Ca$_{0.3}$MnO$_3$, have complex phase diagrams with many competing states. Among the knobs that can be used to control their properties are magnetic field and strain. Hong et al. placed membranes of La$_{0.7}$Ca$_{0.3}$MnO$_3$ on a flexible polymer layer (see the Perspective by Beekman). Stretching the flexible layer resulted in large strains of up to 8% on the membrane. By varying the magnitude and direction of the strain, the researchers were able to explore the phase diagram of the system and influence its magnetic and transport properties.

Science, this issue p. 71; see also p. 32

ARTICLE TOOLS	http://science.sciencemag.org/content/368/6486/71
SUPPLEMENTARY MATERIALS	http://science.sciencemag.org/content/suppl/2020/04/01/368.6486.71.DC1
RELATED CONTENT	http://science.sciencemag.org/content/sci/368/6486/32.full
REFERENCES	This article cites 44 articles, 5 of which you can access for free http://science.sciencemag.org/content/368/6486/71#BIBL
PERMISSIONS	http://www.sciencemag.org/help/reprints-and-permissions

Use of this article is subject to the Terms of Service